Control of Sinusoidal-Ripple Current in Electric Vehicle Battery Chargers

Mr Vishnuvardhan.V[1] Mr B.Sampath[2]

1Assistant Professor in EEE Department, St. Martin's Engineering College, Secunderabad-500100, INDIA

2Assistant Professor in EEE Department, St. Martin's Engineering College, Secunderabad-500100, INDIA

***Abstract*—This paper proposes a battery charger (BC) for electric vehicles based on sinusoidal-ripple-current (SRC) method. The SRC method is used as an advanced charging-discharging method. On the one hand, the sinusoidal current variations alternately change output active power of the BC, negatively affect AC-side terminal current of the BC, and therefore, cause a power quality problem. On the other hand, the output active and reactive powers must be regulated at constant values without any variations for participation in vehicle-to-grid technology. Thus, a particular topology is suggested and then a control system is precisely designed in order to implement SRC charging-discharging method and adjust the output active and reactive powers for vehicle-to-grid technology without the power quality problem. SRC method can also be used in online electrochemical impedance spectroscopy (EIS) for state of charge and state of health estimation in battery management. The proposed control system can also generate the SRC signals, suitable for online EIS, in a controlled way unlike the recently proposed BCs. The simulation and experimental results demonstrate the effectiveness of the proposed solution.**

***Index Terms*—Battery charger, electric vehicle (EV), impedance spectroscopy, sinusoidal-ripple-current (SRC), vehicle-to-grid (V2G).**

I. Introduction

ELECTRIC vehicles (EVs) as one of the elements connected to microgrids (MGs) have drawn a great deal of attention in recent years. Although a large number of EVs may pose a threat to power quality and stability of MGs, they have enough potential to be used as distributed energy storage units. Bidirectional active and reactive power transfer through their battery chargers (BCs) is called vehicle-to-grid (V2G) technology which provides many ancillary services such as load leveling and voltage regulation [1]–[3]. On the other hand, degradation of their battery during V2G technology makes it inconvenient and less preferable unless the battery performance and lifetime are under warranty. Thus, the BCs should be designed based on a fast high-quality charging-discharging method in order to improve the battery performance and lifetime.

Manuscript received September 24, 2019; revised March 17, 2020; accepted April 30, 2020. Date of publication May 12, 2020; date of current version July 16, 2020. The review of this article was coordinated by Dr. M. Vasic. *(Corresponding author: Mahdi Bayati.)*

Mahdi Bayati, Mehrdad Abedi, and Gevork B. Gharehpetian are with the Department of Electrical Engineering, Amirkabir University of Technology, Tehran 1591639675, Iran (e-mail: bayati.mahdi@aut.ac.ir; abedi@aut.ac.ir; grptian@aut.ac.ir).

Maryam Farahmandrad is with the Department of Electrical Engineering, Bu-Ali Sina University, Hamedan 6517833131, Iran (e-mail: m.farahmandrad@alumni.basu.ac.ir).

Digital Object Identifier 10.1109/TVT.2020.2994269

Some charging-discharging methods for Li-ion batteries such as constant-current constant-voltage (CC-CV) [4], pulse current [5], pulse voltage [6], [7], Reflex [8], [9], and sinusoidal-ripple-current (SRC) [10], [11] have already been proposed. The SRC charging-discharging method applies a sinusoidal current with the non-zero average value I_0 and the frequency f_c at which the battery impedance obtains its minimum magnitude until the battery reaches the maximum permissible voltage V_0 [10], [11]. Experiments in [10] and [11] have proved that an optimal *charging* and *discharging* performance, respectively, can be obtained at f_c. Charging time, discharging capacity, charging and discharging efficiency, maximum rising temperature, and lifetime of Li-ion batteries are improved in comparison to CC-CV charging and CC discharging methods [10], [11]. Dynamic charge acceptance is a parameter to measure the battery ability to absorb electrical charge in relation to its capacity. This parameter is particularly important in the case of EVs. In [12], the authors have revealed that SRC method can significantly improve this parameter and the efficiency of the charge acceptance even over 50 percent in lead-acid batteries. In [13], [14], the authors have suggested it as an effective method for reviving Li-ion batteries and prolonging their cycle life. In [15], it improves uniformity of lithium deposition and consequently leads to better cycling stability. In [16], hybrid and conventional SRC methods improve the efficiency and energy transfer of Li-ion battery. In [17], [18], the authors illustrate that it noticeably improves the efficiency and charging time and decreases temperature in Li-ion battery. In [19] and [20], the benefits of SRC method to Li-ion and lead-acid batteries have been explained. In [21], [22], and [23], three single-stage battery chargers have been designed, considering that it has no harmful effects.

As a consequence of the sinusoidal current variations in SRC charging-discharging method, the waveform of delivered or extracted power has a sinusoidal shape. Such variations negatively affect the main power source, for instance, a MG, a DC distribution network, or a fuel cell. In the case of a BC connected to a MG through an AC-DC converter, such variations alternately change output active power of the BC, negatively affect the AC-side terminal current of the BC, and therefore, cause a power quality problem. On the other hand, the output active and reactive powers must be regulated at constant values without any variations for participation in V2G technology like what has been proposed in [24]. Thus, particular importance should be given to this power quality problem.

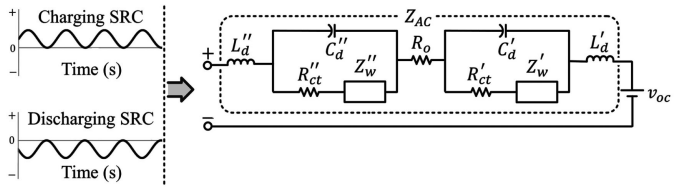

Fig. 1. Complete AC-impedance model of Li-ion battery.

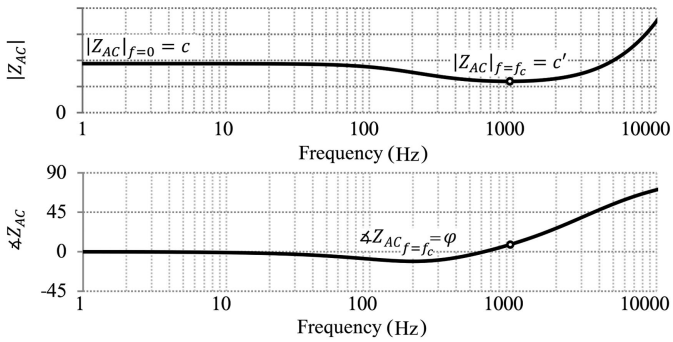

Fig. 2. Frequency spectrum of the AC impedance of Li-ion battery.

The *purpose* of this paper is to propose an EV BC based on SRC charging-discharging method which is able to participate in V2G technology without the mentioned power quality problem. This problem is examined in this way for the first time. The *novelty* of this paper is that an innovative way to resolve the mentioned power quality problem is suggested. Additionally, a new precisely-designed control system is proposed for the EV BC. This control system is able to charge and discharge the battery based on various algorithms like CC-CV, but the results focus on only SRC method. The electrical circuits for SRC method introduced in the main references of this research study have dissipative elements due to their embedded resistances [10], [11]. They cannot be utilized in high-power applications, because they have not been designed based on power electronics, while the proposed EV BC has been founded on power electronics and can be redesigned for many high-power applications such as EV charging stations and even the BCs which do not pertain to EVs.

II. Applications of SRC Method

A. Charging and Discharging

Fig. 1 depicts complete AC-impedance model of Li-ion battery. Fig. 2 depicts the frequency spectrum of Z_{AC}. From the viewpoint of electrical circuit, different charging-discharging frequencies change its magnitude and phase such that it has a minimum magnitude at a particular frequency. To make SRC method, the reference command of the battery current must be defined for the control system as [10], [25]:

$$i_B^* = i_{DC}^* + i_{AC}^* = I_0 + I_1 \cos(2\pi f_c t). \quad (1)$$

The superscript $*$ denotes the reference command. I_0 and I_1 are constant amplitudes. I_0 is positive in charging mode and negative in discharging mode. The instantaneous power is calculated as:

$$P_B = v_B \times i_B^* = v_B (I_0 + I_1 \cos(2\pi f_c t)). \quad (2)$$

Fourier series of the periodic waveform of i_B in (1) consists of two components, a zero frequency component and a cosine component with the frequency f_c. These components also appear in Fourier series of P_B in (2). f_c is tuned in practice [19], [20].

B. Electrochemical Impedance Spectroscopy

On the one hand, SRC is used as a charging-discharging method. Studies on advantages [10]–[20] and disadvantages [26], [27] of this method (only charging, not discharging) are underway and it is still an open research area. On the other hand, it also has other applications in reviving Li-ion batteries and prolonging their life cycle [13], [14] or online electrochemical impedance spectroscopy (EIS) [28]. The EIS is a powerful analysis to measure the battery impedance and the subsequent parameters such as state of charge (SOC) and state of health (SOH) which are useful means of representing the battery conditions. Online EIS is divided into some categories [28]. One of them focuses on measurement through power electronic converters [25], [28]–[30]. An open-loop control system with sinusoidal duty-cycle perturbation for a half-bridge converter, a closed-loop control system with sinusoidal duty-cycle perturbation for a full-bridge phase-shift converter, and a closed-loop control system with step duty-cycle perturbation for a full-bridge converter have been employed in [25], [29], [30], respectively, to create the desired battery voltage and current waveforms. These waveforms are imported into the online EIS algorithms in order to calculate the battery parameters. In conclusion, SRC method is used as a part of online EIS algorithms [25], [28]–[30].

In addition to the main purpose of this paper, the proposed closed-loop control system of the EV BC can be utilized in order to generate the SRC or step signals, suitable for advanced online EIS algorithms, in a *controlled* way. This matter also creates *novelty*:

- An open-loop control system with sinusoidal duty-cycle perturbation has been employed in [25] to supply the online EIS algorithms. Small changes in resistances of the elements and dynamics of the upper and lower voltages in a DC-DC converter completely change its operating point, that is to say, duty cycles of the switches. So, an open-loop control system is not highly reliable in extensive use, especially for EVs. But, a particular closed-loop control system, unlike the open-loop control system in [25], is proposed in this paper.
- Closed-loop control systems with perturbation have been employed in [29] and [30] to supply online EIS algorithms. Perturbation, especially in a wide range of frequencies, threatens the stability of closed-loop systems. In this paper, the SRC or step signals, suitable for advanced online EIS algorithms, are defined as reference commands of the control system, not as perturbation.
- It is common for BCs and charging stations of EVs to use a DC-DC converter whose upper voltage is provided by a DC distribution network [31] or a DC-AC converter [2],

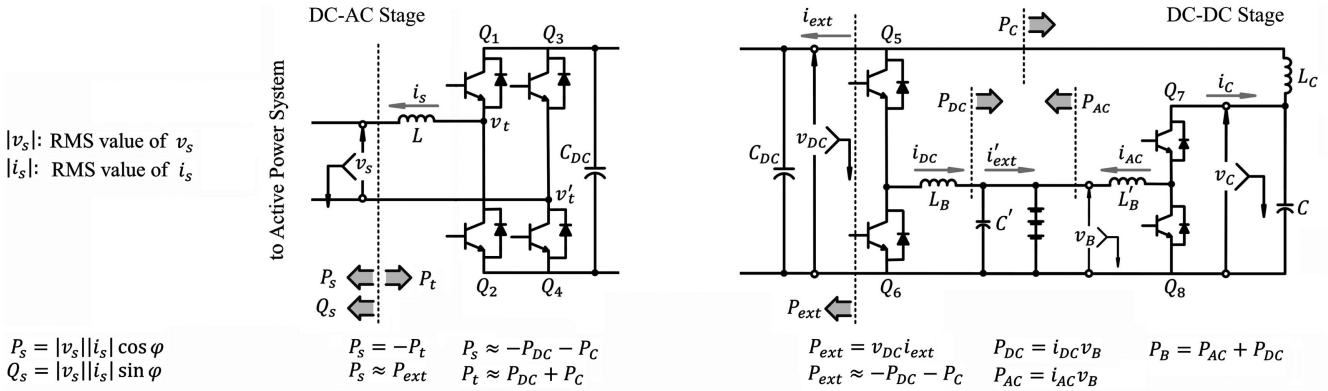

Fig. 3. Power electronic topology of the EV BC.

[8], [9], [16], [32], [33]. Here the upper voltage is DC link voltage (v_{DC}) and the lower voltage is the battery voltage (v_B). In [30] and [25], the upper voltage has been controlled and changed by the DC-DC converter to indirectly make the desired battery current and voltages for the online EIS algorithms. The scenarios presented in [30] and [25] are not very close to reality, because the upper voltage has been changed by the DC-DC converter and also, the online EIS algorithms are independent of the charging-discharging procedure. But, in this paper, it is assumed that the upper voltage (v_{DC}) is fixed, controlled, and provided by the DC-AC converter and then, the desired battery current and voltages for the online EIS algorithms are directly generated in the lower-voltage side, that is, the battery side. The online EIS algorithms and how the battery current and voltage waveforms are processed fall outside the scope of this paper.

III. System Description

A. Power Electronics Topology

Fig. 3 proposes the configuration of the EV BC based on SRC charging-discharging method. It consists of DC-AC and DC-DC stages on the left-hand side and the right-hand side of C_{DC}, respectively, and a control system to have the desired results. The former is called single-phase two-level full-bridge converter and the latter is an innovative combination of two legs, two capacitors, and three inductors. Fig. 4 presents general overview of the control system. The DC-AC stage with its control system shown in Figs. 3 and 4(a) makes a regulated DC link in a predetermined power factor in order to provide power from the MG for the DC-DC stage in charging mode and deliver power from the DC-DC stage to the MG in discharging mode. The DC-DC stage with its control system shown in Figs. 3 and 4(b) charges and discharges the battery based on SRC method.

As shown in Fig. 4(a), the control system of the DC-AC stage regulates Q_s at Q_s^* and v_{DC} at v_{DC}^* to make a regulated link in a predetermined power factor. This means that DC link voltage is controlled by the MG. In V2G technology, each EV must have constant output active and reactive powers which are determined by the MG central controller. The output reactive power Q_s is

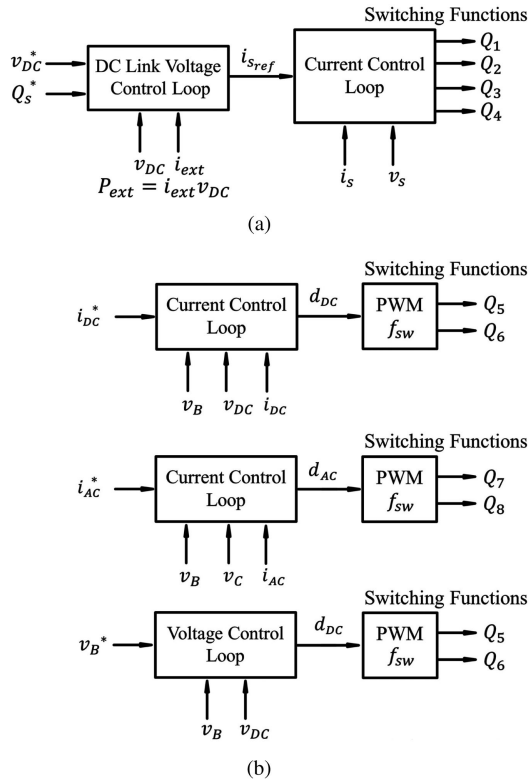

Fig. 4. General overview of the control system of (a) the DC-AC stage (b) the DC-DC stage.

controlled by this control system. If switching and conduction losses are neglected, the output active power P_s equals P_{ext}, the power injected to C_{DC} by the DC-DC stage. i_{ext} is considered as disturbance. The topology of the DC-AC stage is very well-known and has been widely studied in many recent works [2], [32], [34], [35]. Therefore, it is not worth studying again and so, this research focuses on only the DC-DC stage.

As shown in Figs. 4(b) and 5, the control system of the DC-DC stage regulates i_{DC} at i_{DC}^* (I_0) by means of the leg Q_5Q_6 and i_{AC} at i_{AC}^* ($I_1 \cos\omega_c$) by means of the leg Q_7Q_8 until the battery reaches the maximum permissible voltage. Then, it keeps the

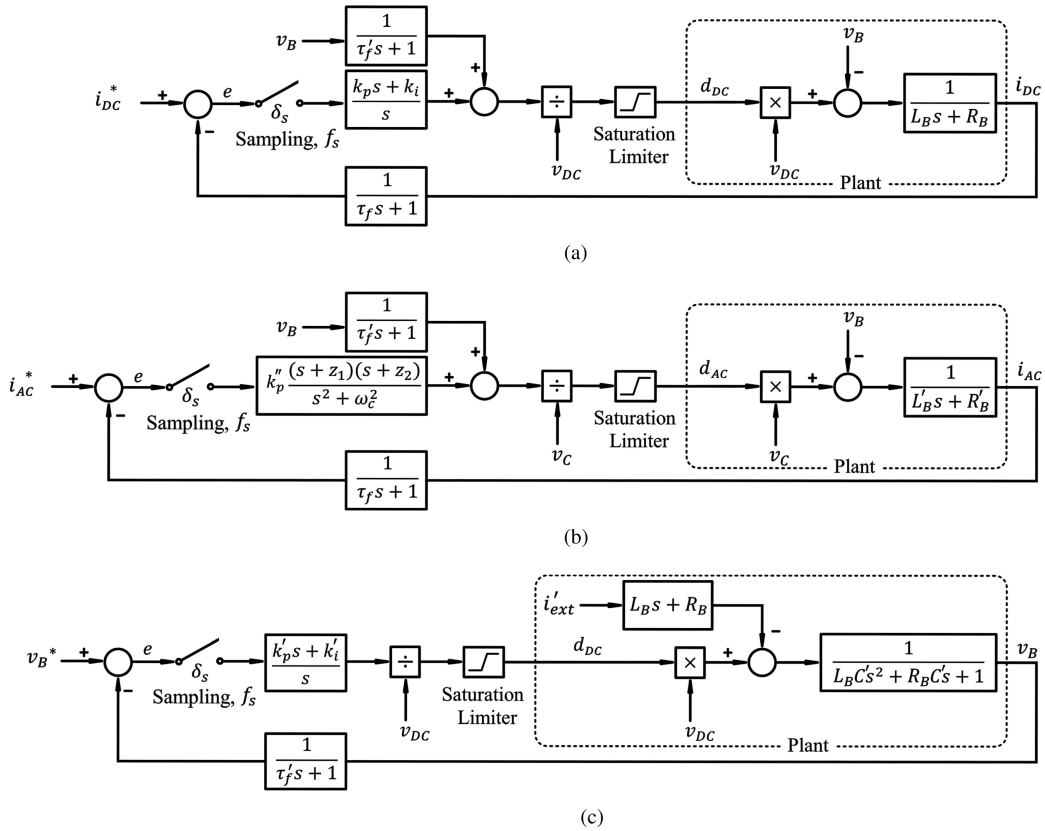

Fig. 5. Detailed overview of the voltage and current control loops in Fig. 4(b) with the plants. (a) DC current control system (b) AC current control system (c) Voltage control system.

battery voltage v_B at v_B^* (V_0) by means of the leg Q_5Q_6. In other words, the two legs work as independent current sources whose magnitudes are I_0 and $I_1 \cos \omega_c$ until the battery reaches the maximum permissible voltage. Then, one leg works as a voltage source whose magnitude is V_0 and one leg is completely turned off.

B. Equations of the Plants

The leg Q_5Q_6 with its inductor can be described in time domain as:

$$-d_{DC}v_{DC} + L_B\frac{di_{DC}}{dt} + R_B i_{DC} + v_B = 0 \tag{3}$$

and in Laplace domain as:

$$i_{DC} = \frac{v_{DC}}{L_B s + R_B} d_{DC} - \frac{1}{L_B s + R_B} v_B. \tag{4}$$

v_B is considered as disturbance and d_{DC} is considered as control signal [32]. d_{DC} is duty cycle of the upper switch Q_5 and $1 - d_{DC}$ is duty cycle of the lower switch Q_6. R_B is the sum of on-state resistance of the switches and internal resistance of the inductor [32].

The leg Q_7Q_8 with its inductor can be described in time domain as:

$$-d_{AC}v_C + L_B'\frac{di_{AC}}{dt} + R_B' i_{AC} + v_B = 0 \tag{5}$$

and in Laplace domain as:

$$i_{AC} = \frac{v_C}{L_B' s + R_B'} d_{AC} - \frac{1}{L_B' s + R_B'} v_B. \tag{6}$$

v_B is considered as disturbance again and d_{AC} is considered as control signal [32]. d_{AC} is duty cycle of the upper switch Q_7 and $1 - d_{AC}$ is duty cycle of the lower switch Q_8. It is worth mentioning that the leg Q_5Q_6 is connected to C_{DC} and the leg Q_7Q_8 is connected to C and indirectly connected to C_{DC} through L_C. That is why v_C have appeared in (5) instead of v_{DC}. It is interesting to compare (5) with (3). In fact, two scenarios are possible:

- Scenario No. 1
  Connection of the leg Q_7Q_8 to C_{DC}
  If conduction and switching losses are neglected,

$$P_s \approx P_{ext} \approx -P_{DC} - P_{AC} = -P_B. \tag{7}$$

  P_B is the battery power in SRC charging-discharging method.
- Scenario No. 2
  Connection of the leg Q_7Q_8 to C
  If conduction and switching losses are neglected,

$$P_s \approx P_{ext} \approx -P_{DC} - P_C. \tag{8}$$

C and L_f have low resistances. Thus, v_C becomes approximately equal to v_{DC}, a little less than v^*_{DC} in steady-state condition.

The leg Q_5Q_6 with its inductor also works as an independent voltage source and can be described in time domain as:

$$i_{DC} - i'_{ext} = C' \frac{dv_B}{dt} \tag{9}$$

along with (3) and in Laplace domain as:

$$v_B = \frac{v_{DC} d_{DC}}{L_B C' s^2 + R_B C' s + 1} - \frac{(L_B s + R_B)\, i'_{ext}}{L_B C' s^2 + R_B C' s + 1}. \tag{10}$$

i'_{ext} is considered as disturbance and d_{DC} is considered as control signal.

C. Control System and Stability

The control loop in Fig. 5(a) provides d_{DC} for PWM strategy in order to regulate i_{DC} at I_0 by turning Q_5 and Q_6 on and off with the switching frequency f_{sw}. Equation (4) has been shown in the form of a block diagram named plant. There is a proportional-integral controller which generates the control signal. It is passed through a saturation limiter to ensure that the control signal is between 0 and 1. Then, it is divided by v_{DC} to make the loop independent of DC link voltage. Feed-forward compensation, adding v_B to the control signal, has three great benefits, dynamic decoupling between the battery and the other parts, improving start-up transient, and enhancing disturbance rejection capability [32]. The voltages and currents are measured using sensors modelled in the form of the first-order transfer functions with the time constants τ_f and τ'_f.

The control loop in Fig. 5(b) provides d_{AC} for PWM strategy in order to regulate i_{AC} at $I_1 \cos \omega_c t$ by turning Q_7 and Q_8 on and off. Equation (6) has been shown in the form of a block diagram named plant. There is a special controller with two zeros and a pair of complex conjugate poles at ω_c that generates the control signal. It is passed through a saturation limiter and is divided by v_C. In addition, feed-forward compensation has been utilized.

The control loop in Fig. 5(c) provides d_{DC} for PWM strategy in order to regulate v_B at V_0 by turning Q_5 and Q_6 on and off. Equation (10) has been shown in the form of a block diagram named plant. There is a proportional-integral controller which generates the control signal. It is passed through a saturation limiter and is divided by v_{DC}.

Open-loop frequency responses of all the three loops in Fig. 5 are shown in Fig. 6. Positive gain and phase margins in Fig. 6 confirm that the minimum-phase systems of Fig. 5 are stable. The closed-loop frequency responses of all the three loops, i_{DC}/i^*_{DC} and i_{AC}/i^*_{AC} and v_B/v^*_B, along with the closed loop frequency response of the disturbance, v_B/i_{ext}, are shown in Fig. 7.

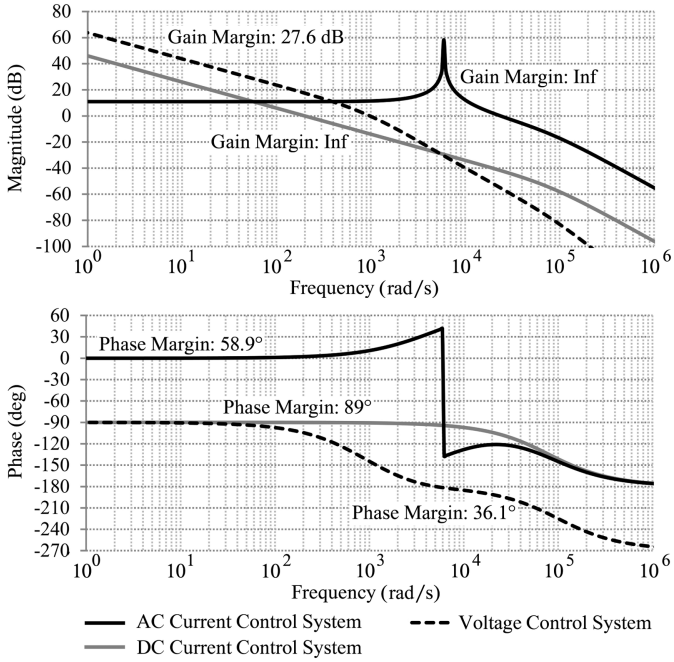

Fig. 6. Open-loop frequency responses.

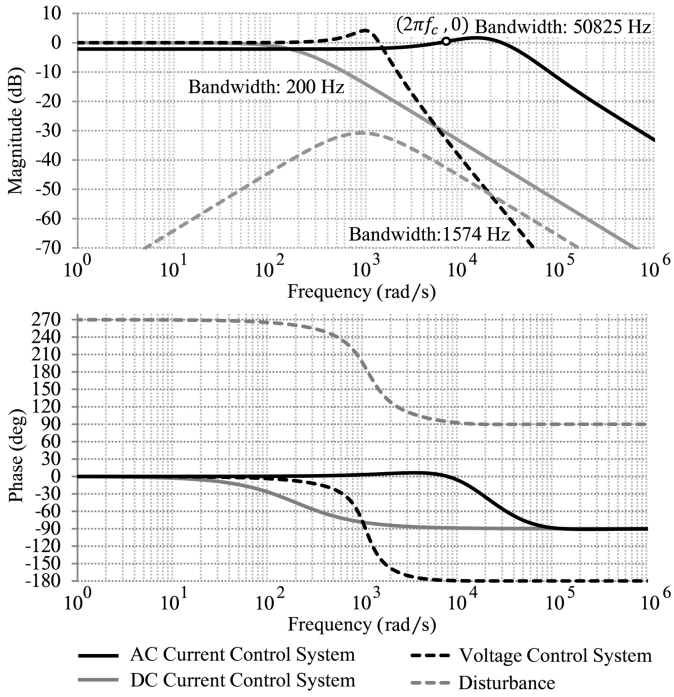

Fig. 7. Closed-loop frequency responses.

IV. Technical Considerations

A. Controllers

In general, to follow a reference command with zero steady-state error, the unstable poles of Laplace transform of the reference command must be included in the controller [32]. Thus, the controller of the loop in Fig. 5(a) successfully tracks a step reference command like I_0 with zero steady-state error because it includes an integral term. To have a closed-loop system with the time constant τ_0 and cancel the stable pole of the plant in order to remove the slow natural response, k_p and k_i must be selected as L_B/τ_0 and R_B/τ_0, respectively [32]. Here, τ_0 is 5 ms and the bandwidth equals 200 Hz. Fig. 7 confirms such a bandwidth which should be far enough from f_{sw}, at least

10 times smaller than f_{sw}. The points 0 dB and 0° at 0 Hz in Fig. 7 reveal that it successfully follows step functions without magnitude attenuation and phase delay.

The controller of the loop in Fig. 5(b) successfully tracks a sinusoidal reference command like $I_1 \cos \omega_c t$ with zero steady-state error because it includes a pair of complex conjugate poles at ω_c. Following sinusoidal reference commands creates many serious challenges [32]. z_1, z_2, and k_p'' are adjusted to make a more stable open-loop frequency response. The points 0 dB and 0° at f_c in Fig. 7 reveal that it successfully follows the sinusoidal function without magnitude attenuation and phase delay.

The PI controller of the loop in Fig. 5(c) successfully tracks a step reference command like V_0 with zero steady-state error because it includes an integral term. The points 0 dB and 0° at 0 Hz in Fig. 7 reveal that it successfully follows step functions without magnitude attenuation and phase delay. k_p' and k_i' are adjusted so that the control system is stable and the effect of i_{ext}' on v_B is minimized. Fig. 7 confirms that the disturbance has a small effect on the output, the point -30 dB at 1 kHz.

B. Adaptive Tuning of f_c

Fig. 2 indicates the frequency f_c at which the battery impedance obtains its minimum magnitude (c'). It varies from battery to battery and varies as a consequence of SOC, temperature, and life cycle [36]. f_c has a specific value in the experimental results, because SOC, temperature, life cycle, and other determining factors in f_c do not change during getting and recording the experimental results. Obviously, they change during charging-discharging process. So, f_c must be tuned in accordance with a defined algorithm in the microcontroller.

There is a difference between v_B and v_{oc} in steady-state condition as follows:

$$v_B = i_{DC}\left(Z_{AC}\big|_{f=0}\right) + i_{AC}\left(Z_{AC}\big|_{f=f_c}\right) + v_{oc}. \quad (11)$$

The voltage drop consists of two parts. To find the smallest voltage drop and variations, an index is defined as:

$$\frac{1}{N}\sum_{k=1}^{N}\left(v_B^k\right)^2 \quad (12)$$

where v_B^k is the k^{th} sample of v_B and N is the number of the samples during the period T_c. It is regularly increased and decreased every ten seconds based on 'perturb and observe' technique with a predetermined increment of ± 1 Hz. If the slope is positive, negative increment is selected; otherwise, positive increment is selected. The slope is the ratio of the index changes to the frequency changes [19]. The average of the index for 100 repetitions is calculated and then, the frequency at which the index has the lowest value is suggested for the control system. f_c varies from 800 Hz to 1200 Hz.

C. Current Ripple

i_{DC} and i_{AC} have ripples with the frequency f_{sw}. The amplitude of the ripples is reduced by:

- increase in the inductances of the legs, L_B and L_B'
  If they are increased, volume, weight, and cost increase.

TABLE I
EXPERIMENTAL PARAMETERS

Parameter		Per Unit	Parameter	
P_b	10.96 W	1	f_{sw} f_c	20000 948 Hz
v_b	16.6 V	1	C C'	11.2 0.2 mF
i_b	0.66 A	1	k_p k_i	0.4 1535.4
I_0 I_1	0.66 A	1.000	k_p' k_i' k_p''	0.4 1535.4 44.67
V_0	16.8 V	1.012	c	0.47 Ω
v_{oc}	16.6 V	1.000	τ_f	1/(80000) s
R_B	7.68 Ω	0.305	τ_f'	1/(100000) s
R_C	1.5 Ω	0.060	z_1 z_2	3104 6951
R_B'	6.78 Ω	0.270	L_B'	1 mH
v_{DC}^*	24 V	1.446	L_B L_C	2 mH

TABLE II
SIMULATION PARAMETERS

Parameter		Per Unit	Parameter		Per Unit
P_b	7987 W	1	v_{oc}	448.20	1
v_b	448.20 V	1	v_s	240 V	0.757
i_b	17.82 A	1	I_0 I_1	17.82 A	1
V_0	453.60 V	1.012	v_{DC}^*	648 V	1.446

- decrease in the upper voltages of the legs, v_{DC} and v_C
  Firstly, if v_{DC} is decreased and, in turn, v_C is decreased, switching losses for each leg, modelled as a current source parallel with each leg, decrease [32]. Secondly, cost decreases because capacitors and switches with lower voltage limits are bought. Thirdly, the control loops work nearer to saturation condition. This undesired condition occurs when duty cycle for each leg becomes more than one. In fact, v_{DC} or v_C are not strong enough in even duty cycles near 100 percent to impose the reference currents. The maximum current that can be injected to the battery is limited by the upper voltage and the sum of on-state resistance of the switches and internal resistance of the inductor in each leg. Decrease in the upper voltage is not good because it may work under the saturation condition.
- increase in the switching frequency, f_{sw}
  Firstly, if it is increased, switching losses increase. Secondly, faster switches are needed and, in turn, it increases cost. f_{sw} must be greater enough (at least 10 times) than f_c to have a relatively pure sinusoidal shape.

There are other trade-offs. However, the parameters are selected so that cost, weight, volume, and losses are minimized.

V. RESULTS

The DC-DC stage of Fig. 3 with a kind of DC-AC stage, widely available at the market, has been implemented in practice according to Table I. Fig. 8 shows the practical setup of the EV BC and Fig. 9 shows the main electronic components in this project. On the other hand, the proposed EV BC in Fig. 3 has been simulated in Matlab Simulink according to Table II. P_b, v_b, and i_b are the power, voltage, and current bases, respectively. Both of the voltage and current bases in Table I are exactly 27 times smaller than those in Table II. So, the power base in practice is 27×27 times smaller. A small prototype has been practically

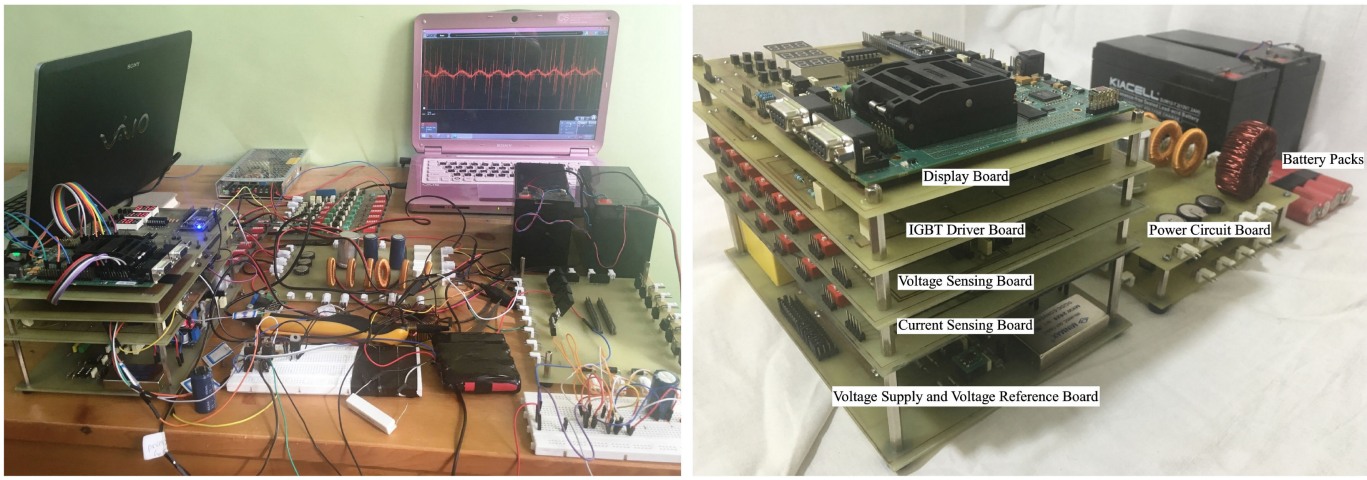

Fig. 8. Practical setup.

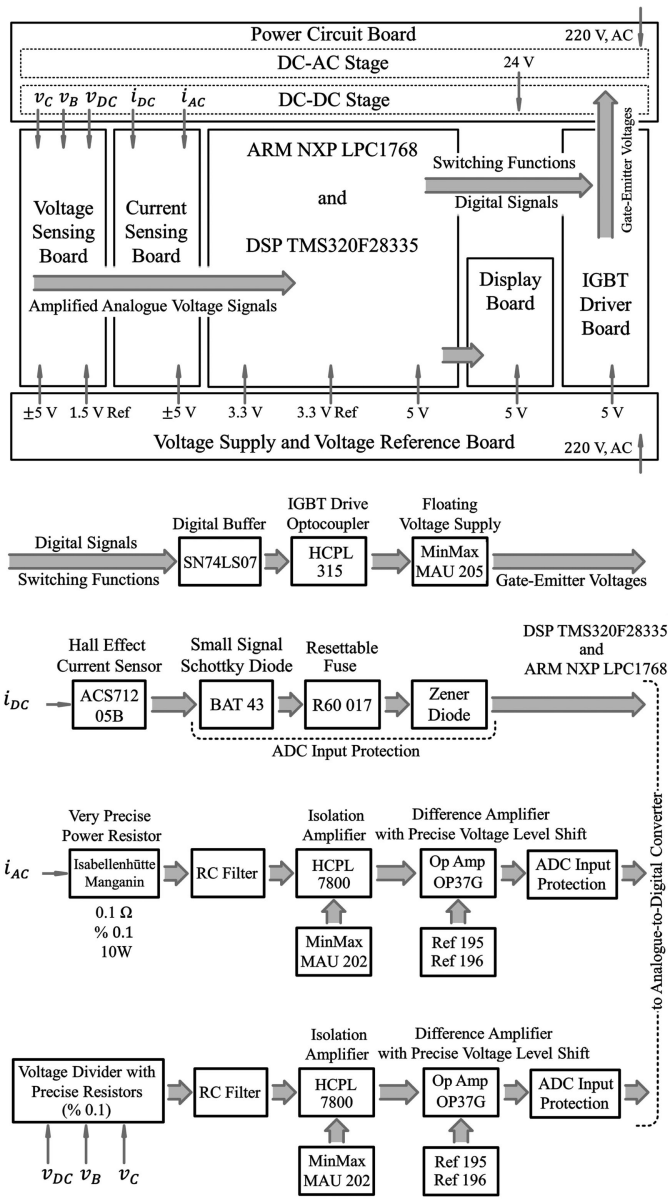

Fig. 9. Diagram of the main utilized electronic components.

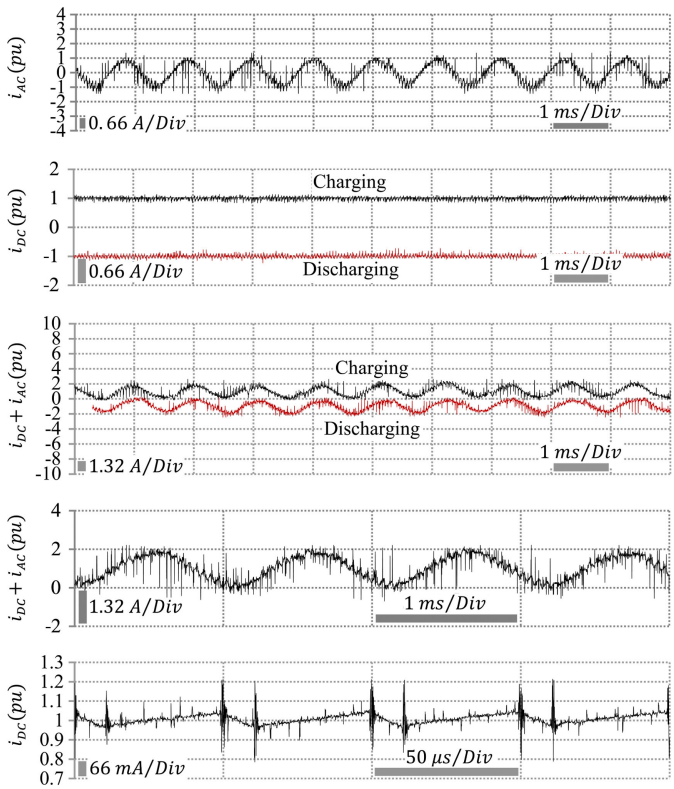

Fig. 10. Important experimental current waveforms.

implemented to decrease cost (this project is not funded by anyone) and avoid danger of electric shock in laboratory. It also means that the impedance bases in practice and simulation are exactly equal because both of the practical voltage and current bases have been equally decreased 27 times, that is, exactly the same simulated system on a smaller scale in practice.

A. *Practical Results*

Experimental results are split into three parts (see Figs. 10 to 12). Fig. 10 shows important current waveforms. f_c was replaced with 948 Hz. Also, I_0 and I_1 were replaced with ±0.66 A or

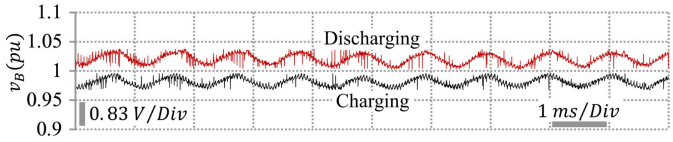

Fig. 11. Important experimental voltage waveforms.

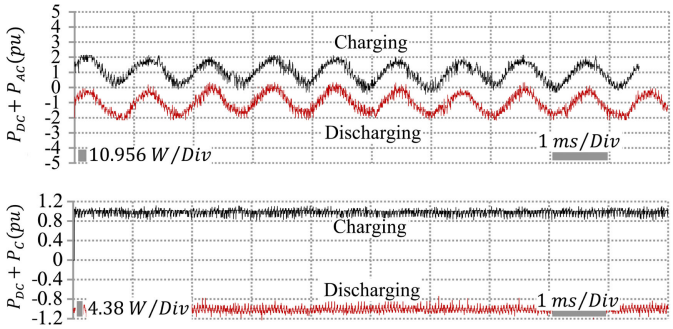

Fig. 12. Important experimental power waveforms.

± 1 pu, positive in charging mode and negative in discharging mode. All of the waveforms in Fig. 10 confirm that the control system successfully follows the reference commands. i_{AC} has a sinusoidal shape with the frequency 948 Hz and the amplitude 1 pu. i_{DC} is constant, 1 pu in charging mode and -1 pu in discharging mode. $i_{DC} + i_{AC}$, in other words, i_B has a sinusoidal shape with the same frequency and amplitude shifted up by 1 pu in charging mode and shifted down by 1 pu in discharging mode. This waveform has been depicted in two different time-scales. The last waveform shows i_{DC} with a short time-scale, 50 μs, to reveal that switching with the frequency 20 kHz takes place.

The main amplitude of i_{DC} equals 1 pu and the amplitude of the ripple is less than 0.1 pu, less than 10 percent of the main amplitude. The current and voltage ripple is an inevitable consequence of using power electronic topologies. As previously mentioned, the current base is 27 times greater in the real prototype. Thus, i_{DC} becomes 27 times greater. This means that the percentage of the current ripple does not change and the main prototype is the same as the small-scale prototype, but 27 times greater. It is worth mentioning that an awful oscilloscope has been used to get the experimental results. Unfortunately, it displays and records them with a lot of noise and with a lot of unreal drastic variations, especially in high-frequency oscillations.

Fig. 11 shows important voltage waveforms. The open-circuit battery voltage, v_{oc}, was equal to 16.6 V during getting results and has been considered as voltage base, 1 pu (see Table I). As formulated in (11), v_B has sinusoidal variations due to i_{AC} and the battery impedance at f_c. It is shifted up in charging mode and is shifted down in discharging mode due to i_{DC} and the battery impedance at 0 Hz. This is in agreement with the waveform in Fig. 11.

Fig. 12 shows important power waveforms. The first waveform, $P_{DC} + P_{AC}$, is the power injected to the battery by the legs Q_5Q_6 and Q_7Q_8 based on SRC charging-discharging method. $P_{DC} + P_{AC}$ equals P_B. P_{DC} is constant, 1 pu in

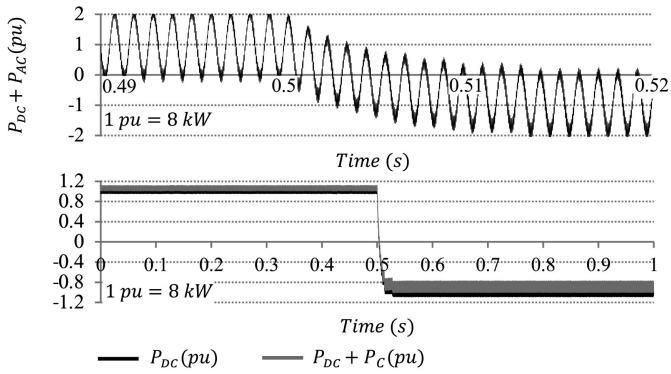

Fig. 13. Important simulated power waveforms.

charging mode and -1 pu in discharging mode. $P_{DC} + P_{AC}$ has a sinusoidal shape with the frequency 948 Hz and the amplitude 1 pu, shifted up by 1 pu in charging mode and shifted down by 1 pu in discharging mode. Two possible scenarios have been defined in subsection III-B:

- Scenario No. 1
  The leg Q_7Q_8, which has the duty to make i_{AC} and P_{AC}, is directly connected to C_{DC}. If L_C becomes short circuit and C is removed in Fig. 3, this type of connection is reached. $-P_s$ and $-P_{ext}$ become approximately equal to $P_{DC} + P_{AC}$ or P_B (see Eq. (7)). As shown in Fig. 12, $P_{DC} + P_{AC}$ has a sinusoidal component as much as its DC component and can alternately change P_s and i_s. The power quality problem, the existence of a harmonic with the frequency f_c and the amplitude as much as the main DC component, can be effectively solved if the *second scenario* is employed.
- Scenario No. 2
  The leg Q_7Q_8, which has the duty to make i_{AC} and P_{AC}, is directly connected to C, not C_{DC}. Fig. 3 shows such a connection. Not directly connecting the leg Q_7Q_8 to C_{DC}, unlike the previous scenario, changes the value of $-P_s$ and $-P_{ext}$. It approximately equals $P_{DC} + P_C$. This power does not have the alternating term, P_{AC}, unlike the previous scenario (see Eq. (8)). P_{AC} causes the power quality problem in P_s and i_s. It can even appear in a different way when the power source is not a DC-AC converter supplied by a MG. It may be even a fuel cell or a DC distribution network. The research studies [31], [37] are the examples of this condition, when the power source is a fuel cell or a DC distribution network.

B. Simulation Results

The simulation results in Fig. 13 are the same as the corresponding experimental results in Fig. 12. P_s^* is changed from -8 kW to 8 kW at 0.5 s. Positive P_s^* discharges and negative P_s^* charges it based on SRC charging-discharging method. Fig. 14 shows the output AC-side terminal current, i_s, for the two possible scenarios presented in subsection III-B. As explained in the previous paragraph, the waveform of i_s has a harmonic with the frequency 948 Hz when the first scenario is employed. This harmonic is removed in the waveform of i_s when the second

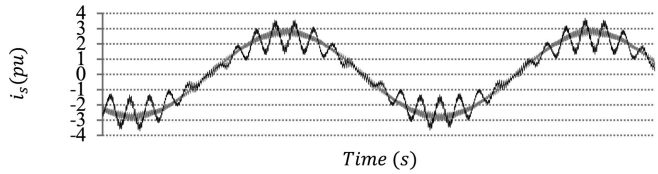

Fig. 14. AC-side terminal current for the two scenarios.

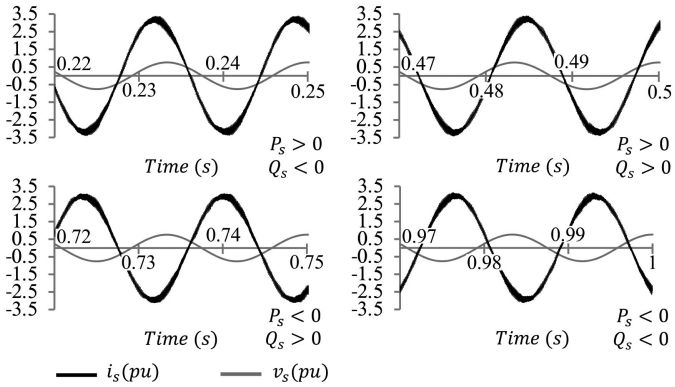

Fig. 15. Participation in V2G technology.

scenario is employed. This means that the power quality problem has been solved. In Fig. 15, Q_s^* is changed from -5 kVAR to 5 kVAR at 0.25 s and vice versa at 0.75 s. P_s^* is changed from 8 kW to -8 kW at 0.5 s. P_s^* and Q_s^* are independently set to validate the flexibility of the control system in switching among all the four quadrants of $P_s - Q_s$ plane.

The power transferred from the MG to the battery in charging mode or vice versa in discharging mode has different values in the two scenarios.

- Scenario No. 1
  The experimental and simulated waveforms of $P_{DC} + P_{AC}$ have been shown in Fig. 12 and Fig. 13, respectively. It has considerable sinusoidal variations, a harmonic with the frequency 948 Hz. This power definitely causes power variations in the AC-side terminal current . This fact is in agreement with what has been shown in Fig. 14 where the harmonic with the frequency 948 Hz has noticeably appeared.
- Scenario No. 2
  The experimental and simulated waveforms of $P_{DC} + P_C$ have been shown in Figs. 12 and 13, respectively. These waveforms have not sinusoidal variations and do not definitely lead to sinusoidal power variations in the AC-side terminal current and P_s. This fact is in agreement with what has been shown in Fig. 14 where the harmonic with the frequency 948 Hz has been removed. In conclusion, this paper proposes an EV BC being able to impose adaptive SRC charging-discharging method without the mentioned power quality problem. The generated current and voltage waveforms can be also inserted to the online EIS algorithms.

Discussion about charging-discharging time, maximum rising temperature, lifetime etc. fall outside the scope of this work.

VI. Conclusion

The simulation and experimental results confirmed that the proposed EV BC with its precisely designed control system can successfully implement SRC charging-discharging method. It is true to state that it can implement even other methods such as CC-CV, pulse-current, and Reflex because the reference commands are defined in general forms. For instance, the pulse-current method is imposed on the battery if I_1 equals zero and I_0 alternately changes from a constant value to zero and vice versa.

Also, an innovative effective solution to resolve the power quality problem was suggested so that it is able to participate in V2G technology and exchange active and reactive power without fluctuation. The proposed DC-DC stage can be separately utilized in charging stations and DC distribution networks providing services for EVs. Moreover, it can generate the SRC or step signals, suitable for advanced online EIS algorithms, in a controlled way.

References

[1] M. Yilmaz and P. T. Krein, "Review of the impact of vehicle-to-grid technologies on distribution systems and utility interfaces," *IEEE Trans. Power Electron.*, vol. 28, no. 12, pp. 5673–5689, Dec. 2013.

[2] M. Yilmaz and P. T. Krein, "Review of battery charger topologies, charging power levels, and infrastructure for plug-in electric and hybrid vehicles," *IEEE Trans. Power Electron.*, vol. 28, no. 5, pp. 2151–2169, May 2013.

[3] M. Bayati, M. Abedi, G. B. Gharehpetian, and M. Farahmandrad, "Short-term interaction between electric vehicles and microgrid in decentralized vehicle-to-grid control methods," *Protection Control Modern Power Syst.*, vol. 4, no. 1, pp. 1–11, 2019.

[4] A. A.-H. Hussein and I. Batarseh, "A review of charging algorithms for nickel and Lithium battery chargers," *IEEE Trans. Veh. Technol.*, vol. 60, no. 3, pp. 830–838, Mar. 2011.

[5] Y. Gao, X. Zhang, Q. Cheng, B. Guo, and J. Yang, "Classification and review of the charging strategies for commercial Lithium-Ion batteries," *IEEE Access*, vol. 7, pp. 43511–43524, 2019.

[6] L.-R. Chen, "A design of an optimal battery pulse charge system by frequency-varied technique," *IEEE Trans. Ind. Electron.*, vol. 54, no. 1, pp. 398–405, Feb. 2007.

[7] L.-R. Chen, "Design of duty-varied voltage pulse charger for improving Li-ion battery-charging response," *IEEE Trans. Ind. Electron.*, vol. 56, no. 2, pp. 480–487, Feb. 2009.

[8] L.-R. Chen, N.-Y. Chu, C.-S. Wang, and R.-H. Liang, "Design of a Reflex-based bidirectional converter with the energy recovery function," *IEEE Trans. Ind. Electron.*, vol. 55, no. 8, pp. 3022–3029, Aug. 2008.

[9] M. Bayati, M. Abedi, H. Hosseinian, and G. B. Gharehpetian, "A novel control strategy for reflex-based electric vehicle charging station with grid support functionality," *J. Energy Storage*, vol. 12, pp. 108–120, 2017.

[10] L.-R. Chen, S.-L. Wu, D.-T. Shieh, and T.-R. Chen, "Sinusoidal-ripple-current charging strategy and optimal charging frequency study for Li-ion batteries," *IEEE Trans. Ind. Electron.*, vol. 60, no. 1, pp. 88–97, Jan. 2013.

[11] L.-R. Chen, J.-J. Chen, C.-M. Ho, S.-L. Wu, and D.-T. Shieh, "Improvement of Li-ion battery discharging performance by pulse and sinusoidal current strategies," *IEEE Trans. Ind. Electron.*, vol. 60, no. 12, pp. 5620–5628, Dec. 2013.

[12] M. Smith, D. Gladwin, and D. Stone, "An analysis of the influence of high-frequency ripple currents on dynamic charge acceptance in lead-acid batteries," *J. Energy Storage*, vol. 22, pp. 27–35, 2019.

[13] P.-T. Chen, F.-H. Yang, T. Sangeetha, H.-M. Gao, and K. D. Huang, "Moderate energy for charging Li-ion batteries determined by first-principles calculations," *Batteries Supercaps*, vol. 1, no. 6, pp. 209–214, 2018.

[14] P.-T. Chen *et al.*, "Reviving aged Lithium-Ion batteries and prolonging their cycle life by sinusoidal waveform charging strategy," *Batteries Supercaps*, vol. 2, no. 8, pp. 673–677, 2019.

[15] Z. Zhang, Z. L. Wang, and X. Lu, "Suppressing lithium dendrite growth via sinusoidal ripple current produced by triboelectric nanogenerators," *Adv. Energy Mater.*, vol. 9, no. 20, 2019, Art. no. 1900487.

[16] S. Hu, Z. Liang, and X. He, "Hybrid sinusoidal-pulse charging method for the Li-ion batteries in electric vehicle applications based on AC impedance analysis," *J. Power Electron.*, vol. 16, no. 1, pp. 268–276, 2016.
[17] H. Vazini, M. Asadi, M. Karimadini, and H. Hajisadeghian, "Sinusoidal charging of Li-ion battery based on frequency detection algorithm by pole placement control method," *IET Power Electron.*, vol. 12, no. 3, pp. 421–429, 2018.
[18] Y.-D. Lee and S.-Y. Park, "Electrochemical state-based sinusoidal ripple current charging control," *IEEE Trans. Power Electron.*, vol. 30, no. 8, pp. 4232–4243, Aug. 2015.
[19] A. A. Hussein, A. A. Fardoun, and S. S. Stephen, "An online frequency tracking algorithm using terminal voltage spectroscopy for battery optimal charging," *IEEE Trans. Sustain. Energy*, vol. 7, no. 1, pp. 32–40, Jan. 2016.
[20] A. A. Hussein, A. A. Fardoun, and S. S. Stephen, "An ultrafast maximum power point tracking technique for optimal battery charging," *IEEE Trans. Sustain. Energy*, vol. 8, no. 3, pp. 1321–1329, Jul. 2017.
[21] S. Li, J. Deng, and C. C. Mi, "Single-stage resonant battery charger with inherent power factor correction for electric vehicles," *IEEE Trans. Veh. Technol.*, vol. 62, no. 9, pp. 4336–4344, Nov. 2013.
[22] O. Kwon, J.-S. Kim, J.-M. Kwon, and B.-H. Kwon, "Bidirectional grid-connected single-power-conversion converter with low-input battery voltage," *IEEE Trans. Ind. Electron.*, vol. 65, no. 4, pp. 3136–3144, Apr. 2018.
[23] H. Zeng, X. Wang, and F. Z. Peng, "High power density Z-source resonant wireless charger with line frequency sinusoidal charging," *IEEE Trans. Power Electron.*, vol. 33, no. 12, pp. 10148–10156, Dec. 2018.
[24] M. Kesler, M. C. Kisacikoglu, and L. M. Tolbert, "Vehicle-to-grid reactive power operation using plug-in electric vehicle bidirectional off-board charger," *IEEE Trans. Ind. Electron.*, vol. 61, no. 12, pp. 6778–6784, Dec. 2014.
[25] W. Huang and J. A. A. Qahouq, "An online battery impedance measurement method using DC-DC power converter control," *IEEE Trans. Ind. Electron.*, vol. 61, no. 11, pp. 5987–5995, Nov. 2014.
[26] S.-Y. Cho, I.-O. Lee, J.-I. Baek, and G.-W. Moon, "Battery impedance analysis considering DC component in sinusoidal ripple-current charging," *IEEE Trans. Ind. Electron.*, vol. 63, no. 3, pp. 1561–1573, Mar. 2016.
[27] A. Bessman *et al.*, "Challenging sinusoidal ripple-current charging of Lithium-Ion batteries," *IEEE Trans. Ind. Electron.*, vol. 65, no. 6, pp. 4750–4757, Jun. 2018.
[28] M. A. Varnosfaderani and D. Strickland, "A comparison of online electrochemical spectroscopy impedance estimation of batteries," *IEEE Access*, vol. 6, pp. 23668–23677, 2018.
[29] Y.-D. Lee, S.-Y. Park, and S.-B. Han, "Online embedded impedance measurement using high-power battery charger," *IEEE Trans. on Ind. Appl.*, vol. 51, no. 1, pp. 498–508, Jan./Feb. 2015.
[30] J. A. A. Qahouq and Z. Xia, "Single-perturbation-cycle online battery impedance spectrum measurement method with closed-loop control of power converter," *IEEE Trans. Ind. Electron.*, vol. 64, no. 9, pp. 7019–7029, Sep. 2017.
[31] M. Tabari and A. Yazdani, "Stability of a DC distribution system for power system integration of plug-in hybrid electric vehicles," *IEEE Trans. Smart Grid*, vol. 5, no. 5, pp. 2564–2573, Sep. 2014.
[32] A. Yazdani and R. Iravani, *Voltage-Sourced Converters in Power Systems*, vol. 34. Hoboken, NJ, USA: Wiley, 2010.
[33] J. Rocabert, A. Luna, F. Blaabjerg, and P. Rodriguez, "Control of power converters in AC microgrids," *IEEE Trans. Power Electron.*, vol. 27, no. 11, pp. 4734–4749, Nov. 2012.
[34] J. Pinto, V. Monteiro, H. Gonçalves, and J. L. Afonso, "Onboard reconfigurable battery charger for electric vehicles with traction-to-auxiliary mode," *IEEE Trans. Veh. Technol.*, vol. 63, no. 3, pp. 1104–1116, Mar. 2014.
[35] T. Tanaka, T. Sekiya, H. Tanaka, M. Okamoto, and E. Hiraki, "Smart charger for electric vehicles with power-quality compensator on single-phase three-wire distribution feeders," *IEEE Trans. Ind. Appl.*, vol. 49, no. 6, pp. 2628–2635, Nov./Dec. 2013.
[36] X. Wei, X. Wang, and H. Dai, "Practical on-board measurement of Lithium Ion battery impedance based on distributed voltage and current sampling," *Energies*, vol. 11, no. 1, pp. 64–79, 2018.
[37] Z. Jiang and R. A. Dougal, "Synergetic control of power converters for pulse current charging of advanced batteries from a fuel cell power source," *IEEE Trans. Power Electron.*, vol. 19, no. 4, pp. 1140–1150, Jul. 2004.